MCU-Based Safer Coagulation Mode by Nonfixed Duty Cycle for an Electrosurgery Inverter

Congbo Bao, *Graduate Student Member, IEEE*, and Sudip K. Mazumder, *Fellow, IEEE*

***Abstract*—The arcing-involved pulsating coagulation mode with both active and blank periods is essential for modern electrosurgery. This article begins with a comprehensive introduction to such a pulsating mode, followed by its implementation challenges. Then, an industrial-scale low-speed microcontroller unit, TMS320F28379D, is utilized to exemplify the proposed output sampling and data-transferring strategy on a gallium nitride (GaN) based high-frequency inverter that enables coagulation mode with interweaved active periods and blank periods. The inverter prototype fills the active period with 390 kHz sinusoids of amplitude ranging from hundreds to thousands of volts, while maintaining null outputs during blank periods. The strategy of sampling the above-mentioned sinusoidal outputs, coupled with their data transfer facilitated by direct memory access, is also articulated for subsequential power computation. Besides that, a novel nonfixed duty cycle approach, featuring an alterable number of sinusoids as the active period, is proposed and integrated into the GaN-based inverter to enhance mode safety. Finally, the power tracking performance of the mode is evaluated initially on resistive load, secondarily on resistive plus capacitive load, and third on fresh biotissue with the appearance of electrical arcing. The existing necessity of the null blank periods is examined at the end of the article.**

***Index Terms*—Coagulation mode, direct memory access (DMA), duty cycle, electrical arcing, electrosurgery, gallium nitride, inverter, microcontroller, safety enhancement, sampling strategy.**

I. Introduction

ELECTROSURGERY is ubiquitous in the operating room for all kinds of surgical treatments due to its versatility and eminent therapeutic effects [1], [2], [3], [4], [5]. The terminology "electrosurgery" refers to a dedicated technique that applies a well-regulated AC voltage of frequency, ranging from 0.2 to 5 MHz, to biological tissue for certain clinical effects, such as cutting and coagulation. The coagulation mode is further subdivided into categories of fulguration, spray, or other customized names by existing electrosurgery generator (ESG) manufacturers [6], [7], [8], [9], [10]. However, there is no significant difference among those names when viewed from an electrical point of view since fulguration and spray both feature pulsating output voltage but different amplitudes. It is worth mentioning that the output voltage level of ESG for the same so-called fulguration or spray is usually high enough to produce electrical arcing, but the exact voltage differs among manufacturers [8], [9], [11]. Therefore, it is called coagulation mode in this article for the sake of simplicity. Nowadays, by integrating cutting, coagulation, or other functional circuitry units into a single equipment case, a commercially available ESG can induce all those effects when operated professionally by surgeons with the assistance of suitable external electrosurgical accessories, such as return pads, forceps, smoke evacuators, electro-scalpels (ES) in all kinds of shapes, and so on [5]. However, those profit-oriented commercial companies publicly release very limited technical details regarding their specific circuitry design or control scheme of ESG that can deliver the aforementioned effects.

There is some literature from academia talking about the detailed circuitry implementation and control for cutting mode. A multiphase interleaved inverter is reported in [12] and regulated by a combined power control method in [13] to ensure constant power delivery for cutting under rapid load dynamics. A two-rail Buck converter with a square-shaped output is developed for fast power tracking [14]. A silicon carbide (SiC)-based inverter is described for wide load impedance under cutting mode [15]. Resonant inverters with sinusoidal outputs are reported in [16] and [17]. It is also reported in the literature that the electrocuting quality induced by the ESGs can refined through different feedback mechanisms, such as thermal information or load impedance [17], [18], [19]. However, literature elaborating on circuitry implementation or control of pulsating coagulation mode is still missing so far [14], [17], [18], [19], [20], [21], [22]. The properly applied coagulation mode is quite helpful for hemostasis, intraoperative hemorrhage reduction in patients, wound sealing, etc. [5], [22], [23]. Therefore, it deserves more attention from researchers to improve its clinical performance or enhance its safety. Meanwhile, more technical details, such as complete electrical design and implementation, control scheme, etc., should be extensively available as reference literature for researchers or anyone with an interest in the topic. Motivated by that, authors sprout a strong sense of mission to investigate the coagulation mode with the target of filling the missed literature gap.

Our previous work centers on cutting mode and conceives a high-frequency inverter (HFI) that enables electrosurgery with

Manuscript received 12 December 2023; revised 17 February 2024; accepted 22 March 2024. Date of publication 29 March 2024; date of current version 16 May 2024. This work was supported in part by the National Institute of Biomedical Imaging and in part by the Bioengineering of the National Institutes of Health under award number R01EB029766. Recommended for publication by Associate Editor M. Ponce-Silva. *(Corresponding author: Sudip K. Mazumder.)*

The authors are with the Department of Electrical and Computer Engineering, University of Illinois Chicago, Chicago, IL 60607 USA (e-mail: cbao5@uic.edu; mazumder@uic.edu).

Color versions of one or more figures in this article are available at https://doi.org/10.1109/TPEL.2024.3383286.

Digital Object Identifier 10.1109/TPEL.2024.3383286

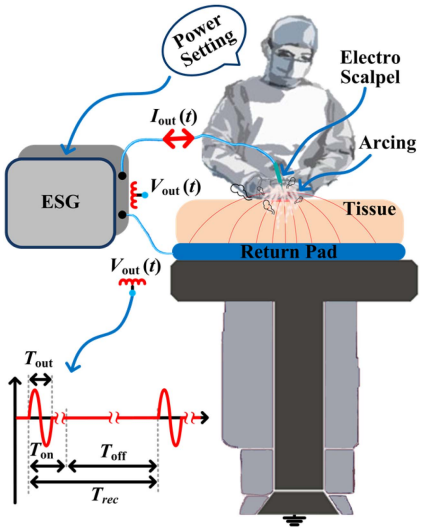

Fig. 1. Graphic demonstration of ESG operating at arcing-involved coagulation mode with pulsating outputs. The electro scalpel is not directly contacting the tissue and the red line crossing the tissue mimics the current path. The sinusoidal output period is represented by $T_{\rm out}$ while the output voltage and current are denoted by $V_{\rm out}(t)$ and $I_{\rm out}(t)$, respectively. The recurring period $T_{\rm rec}$ consists of an active duration $T_{\rm on}$ and a blank duration $T_{\rm off}$. The professional surgeons will set the desired power per the clinical needs and their experience. The ES is usually a blunt metal piece, rather than the sharp surgical knife seen in conventional surgery.

a continuous sinusoidal voltage of 390 kHz. The electrocuting quality induced by the HFI is further improved through power adaptation that is based on temperature on the cutting site or biotissue impedance information [17], [18], [19], [24]. Grounding on the experience accumulated from our prior cutting work, this article herein delves into the circuitry implementation and power control of coagulation mode, with an additional focus on enhancing mode safety. Instead of continuous output seen in cutting mode, the coagulation effect is effectively elicited by a pulsating one, as depicted in Fig. 1. It is illustrated in the bottom-left corner of Fig. 1 that the ESG activates the output for a short time duration ($T_{\rm on}$), and then the output voltage is shut down as a blank period ($T_{\rm off}$) for the rest time of the recurring period ($T_{\rm rec}$). The existence of blank periods is experimentally proved to be critical at the end of the article. The terminology duty cycle ($D_{\rm on}$) is defined by dividing $T_{\rm on}$ by $T_{\rm rec}$ to indicate the percentage of time duration wherein the output of ESG is activated. It is noteworthy that the duty cycle for coagulation mode is a single fixed value in existing commercial ESGs [5], [8]. The peak voltage magnitude in the active period $T_{\rm on}$ is high enough, such that electrical field strength near the tip of the ES exceeds the breakdown level of the air when the tip gets sufficiently close to the biotissue surface. Consequently, the coagulation mode routinely involves electrical arcing that occurs as the air between tissue and ES is ionized by high voltage. The current path is completed through the ionized air, and energy is delivered to the biotissue by plasma even if the ES is held a few millimeters away from the tissue surface. Consequently, instead of direct physical contact, the ES tip can be kept away at a certain distance from the target tissue in coagulation mode. The very high-temperature arcing arrives at the tissue, and then rapidly spreads over a relatively large surface with reduced power concentration or density, thereby, the local temperature of the tissue is continuously raised. The subsequent blank period provides extra time for the tissue to cool down, and thus, the local temperature of liquid content inside the majority of cells is initially maintained below the boiling point, 100 °C. It is reported that the temperature located between 60 °C and 100 °C thermally damages the cell wall, and then the cellular water content in the cytosol will be lost, resulting in macroscopical desiccation and volumetric shrinkage of tissue [5]. This tissue status change is reflected by the increased tissue impedance when evaluated from an electrical property aspect. On the other hand, such a temperature range results in protein denaturation by rupturing the hydrothermal bonds existing among the protein molecules, followed by a randomly reformed gelatinous structure after the initial rupture [5]. In consequence, the coagulation effect is secured whereas the cutting effect by explosive cellular liquid vaporization is almost negligible [19]. Finally, it is important to note that the occurrence of electrical arcing during coagulation is accompanied by high temperatures. Thus, the local temperature of partial biotissue can reach hundreds or thousands of degrees Celsius when the arcing is in contact with tissue or when a plasma current passes through the tissue with increased impedance. Such high temperature causes cellular carbonization and leaves tissue with a black and/or brown hue. Therefore, it always deserves extensive practice or training for surgeons to properly apply coagulation mode, such that it is capable of bridging the gap between tissue surfaces to seal the wound, for instance, opposing sides along the cutting trace, or capable of occluding the blood vessels for hemostasis.

Along with its versatility, it is also quite challenging to implement the coagulation mode, especially with accurate power control and enhanced safety. Some of the reasons are stated as follows. The output is pulsating in this mode, and energy is delivered to the biotissue through electrical arcing which introduces considerable nonlinearity to the circuitry and requires very high-speed analog-to-digital converters (ADC) to accurately sample the arcing-included outputs [19], [25]. High-speed low-latency ADCs are utilized to sample the square waveform output of the cutting mode in [21]. Even with a high-speed field programmable gate array (FPGA), the strategy to reduce the data processing time-consuming is still needed [21]. In [14], the square waveform outputs under cutting mode are sampled by ADCs with a 50-MHz sampling rate and processed by a Xilinx FPGA. The pulsating coagulation mode involves larger arcing than the cutting mode, which significantly distorts the sinusoidal output. In this regard, an even higher sampling rate than the one reported above is required to sense the output signal with precision. In return, the digital microcontroller unit (MCU) operational instruction or computational burden, needed communication throughput, etc., progressively shoots up in order to address the increased ADC sampling points. Besides that, it is worth noting that the fundamental (sinusoidal) output frequency of ESG is, at least, hundreds of kilohertz, and then the output cycle is of short duration ($\sim$2.56 μs herein for the HFI with 390 kHz output). As a consequence, aforesaid digital tasks or

processing are supposed to be finished in a few microseconds for ultra-fast real-time control, making it demanding for the MCU to be used. Apart from what has been mentioned, the output voltage level raises significant concerns about the safety of using such a mode. The reason is that such high-voltage and high-frequency output might contribute to capacitive coupling and cause electrosurgery-related complications, or to the accidental adjacent thermally injured site, etc. Therefore, it is vital to address the safety concerns in the developed coagulation design.

With all these factors in mind, this article investigates and attempts to prototype the coagulation mode using an industrial-scale low-speed MCU. In this prototype, the output power is properly controlled in real-time with high accuracy whereas, except for ADCs contained by the MCU itself, no extra ADCs or data acquisition system is demanded. In addition, the output voltage stress is also reduced through the original proposition of the nonfixed duty cycle control scheme for safety considerations. The main contribution of the article is summarized as follows.

1) A GaN-based hardware prototype is developed for pulsating coagulation mode that features 390 kHz sinusoids in active periods and null output in blank periods.
2) An output sampling strategy using low-speed ADCs, resultant data-transferring tactic using DMA, and corresponding firmware control scheme is originally designed and practically implemented on an industrial-scale low-speed MCU for power regulation of coagulation mode.
3) The power tracking performance of HFI is scrutinized and summarized for resistive load, resistive plus capacitive (R–C) load, and fresh biotissue load.
4) A novel nonfixed duty cycle method, featuring an alterable number of sinusoids in the active period, is proposed to enhance the coagulation mode safety through reduced output voltage stress and diminished terminal leakage current.
5) The existence of the null blank periods for pulsating coagulation is experimentally proved to be a necessity.

Details for deliverables mentioned above are covered hereinafter and the rest of the article is organized as follows. Section II starts with a description of the hardware setup. Then, the proposed nonfixed duty cycle approach, together with output sampling and data transferring strategy, is narrated in detail. Next, Section III captures the controllability of the duty cycle and power tracking performance under resistive load and R–C load. The efficacy of the proposed nonfixed duty cycle is justified in this section as well. After that, Section IV outlines the power tracking performance with biotissue load, and the existing importance of the blank periods is also emphasized here. Finally, Section V concludes this article.

II. Design Considerations

A. Overall Setup Description and Waveform Generation

The employed topology, outputting 390 kHz sinusoidal voltage with low total harmonic distortion (THD), is initially introduced in [17] for cutting mode. It is recaptured in Fig. 2 with a higher turn ratio transformer to further boost the output voltage to the required level for the coagulation mode. The output power

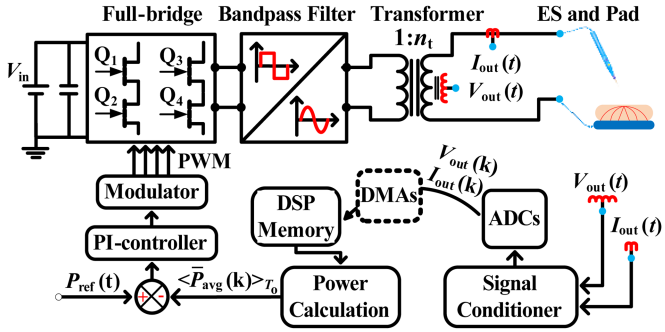

Fig. 2. Schematic and control diagram of the HFI with 390 kHz output [17]. The sensed output signals are processed by the signal conditioning board before they are digitally sampled. Then, the ADCs readings are transferred to storage memory by DMAs for subsequent average power calculation. The transformer turn ratio, n_t, is 8.57 and the electro-scalpel is abbreviated as ES.

is regulated by a proportional-integral (PI) controller where the K_p and K_i are set as 0.05 and 25 000, respectively. The GaN devices (Q_1-Q_4) in the full bridge are GS66508B from Infineon Technologies Canada Inc. (formerly Gan Systems Inc.), and they are under phase shift control. The pulsewidth modulation (PWM) signals that control GaN devices are produced by the TMS320F28379D from Texas Instruments. The dc input is converted into tri-state bipolar square waveforms which are further shaped into a sinusoidal waveform by a bandpass filter detailed in [17]. Owing to the presence of such a filter, the device switching frequency is 390 kHz and the same as the output frequency.

Additionally, the coagulation mode features pulsating outputs, as shown in the bottom-left corner of Fig. 1, thus, the control scheme differs from that of the cutting mode. The hardware implementation of HFI in Fig. 2 is displayed in Fig. 3(a) and the overall system for pulsating coagulation trials is exhibited in Fig. 3(b). Null cycles with zero output, serving as the blank period, are produced by turning off all 4 GaN transistors in the full bridge. The transformer steps up the sinu-soidal voltage and applies it to the biotissue through the ES and return pad. The biotissue is directly placed on the pad with a large contact area to dilute the current density such that the coagulation effect is not induced on the return pad side, but on the ES side. The three-axe gantry is leveraged to hold the ES whenever needed, and the exhauster is installed to remove the small particles or smell if any generated during the electrosurgery. Grounding on the setup in Fig. 3, multitrials are conducted and reported in subsequent sections.

B. Coagulation Mode With Nonfixed Duty Cycle

A single fixed percentage, such as 6.25% or so, is reported as the duty cycle in existing commercial ESGs for coagulation with a ~20 kHz recurring frequency [5], [8], [9], [10]. In other words, the existing ESGs activate the output for 1 cycle ($T_{on} = T_{out}$) and the recurring period has a duration of 16 output cycles for coagulation ($T_{rec} = 16 \cdot T_{out}$), as illustrated in Fig. 4(a). The delivered coagulation mode herein is also configured with a recurring period of 16 output cycles as commercial ESGs. Nonetheless, it is not necessary for the recurring period to be

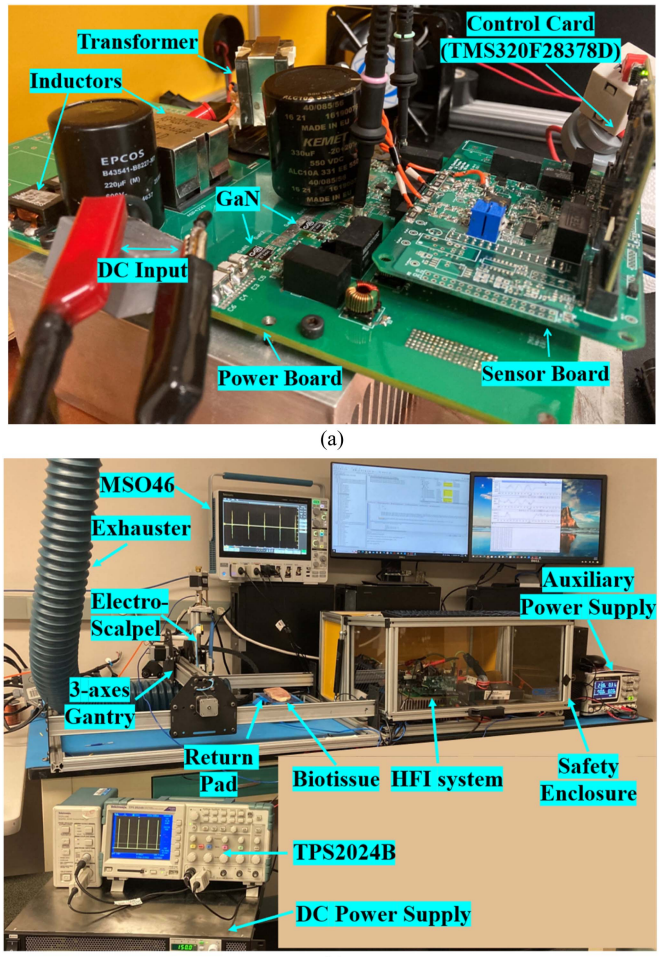

Fig. 3. (a) GaN-based hardware implementation of the HFI. (b) Overall experimental setup for trial testing.

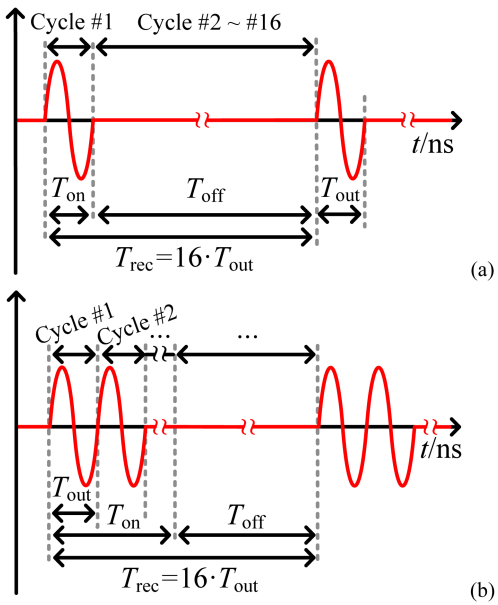

Fig. 4. Illustration of pulsating coagulation mode with (a) a fixed duty cycle by 1 active cycle, and (b) a nonfixed duty cycle by multiple active cycles.

exactly 16 output cycles and it can be set to other values as well. It is a tradeoff between recurring cycle length and the overall coagulation effects. The biotissue can be carbonized because of insufficient cooling by an overshortened recurring period while the coagulation effect cannot be efficiently induced by an over-lengthened period. For this reason, it is important to choose the recurring period. However, the optimum value of the recurring length is not the focus of this article and thus, it is identically set as the value reported in the commercial unit.

As is known, the energy is only delivered to the load in active intervals with the presence of ionized air, and not transported in blank periods. The single active cycle in conventional ESGs rapidly uplifts the output voltage as the desired average power over the entire recurring period increases, and thus, further escalates the safety concerns hinted in the prior section. The boosted voltage not only increases the chance of alternative site thermal injury by virtue of the accident isolation breakdown, but also increases the leakage current and possibility of electrosurgery-related complications. To address the issue related to the single fixed active cycle, a novel nonfixed duty cycle approach is originally proposed here, as portrayed in Fig. 4(b) wherein the ESG is flexibly activated for multicycles, marked as cycle #1 and cycle #2, etc., and then maintained inactive for the rest cycles. The efficacy of such a proposal in terms of reducing output voltage stress and shrinking leakage current for enhanced safety is experimentally justified in Section III-C.

C. Output Sampling and Data-Transferring Strategy

The fundamental output frequency of the HFI has been as high as 390 kHz and the routine occurrence of electrical arcing heavily distorts the outputs, making it a necessity to have ADCs of sufficiently high speed for accurate output sampling. The ultrafast ADC, in return, periodically yields a mass of data that needs to be processed by the MCU cycle-by-cycle for real-time control. However, before those ADC sampling results can be accessed by the MCU central processing unit (CPU), they should be transferred from ADC peripheral result registers and stored in the MCU memory first. The above-mentioned process is conventionally achieved by initiating an ADC interrupt service routine (ISR) and a certain amount of latency is added to the triggering source before the execution of the first instruction in ISR. Then, the CPU exclusively spends a significant amount of time inside the ISR shifting the ADC results data to memory for later post-processing. This data-transferring process should be quickly finished before the ADC results are overwritten by data from the next cycle to avoid losing data. Considering both the output frequency range of electrosurgery and the ADC data points required, it will be time-tight for controllers to handle the ISR on time without a system clock of sub-GHz or more. The MCUs or processors of such high speed are usually of high cost, meanwhile, they are not integrated with the ADC module or many other frequently used peripherals, for instance, the PWM, etc., making them not handy to use.

To tackle that, this article designs a low-speed MCU- and direct memory access (DMA) based regime for output sampling and resultant data transferring. The DMA technique is

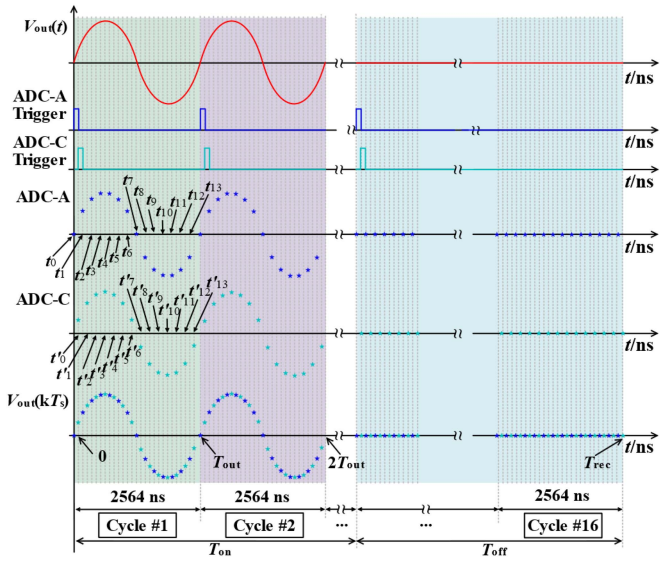

Fig. 5. Design of the oversampling strategy for the output voltage sampled by two low-speed ADCs.

a hardware approach to transfer data between MCU peripherals and memory, and it runs in parallel with the CPU, thereby freeing the CPU for more tasks [26]. The TMS320F28379D is a real-time MCU from the TI C2000 series and it is integrated with various general purposes peripherals, such as ADC, DMA, PWM, etc. So, it is employed herein to trial the designed regime with the ultimate goal of implementing pulsating coagulation mode. This MCU has a system clock of 200 MHz (5 ns per clock cycle) and 43.5-MHz ADC modules (ADC-A∼ADC-D) plus 6 DMA channels (DMA-Ch1∼DMA-Ch6) [26]. All ADC modules work independently, and each module possesses 16 start-of-conversions (SOC), i.e., SOC0-SOC13, which sample signals one by one. ADC-A and ADC-C are assigned in the same group to oversample the output voltage while ADC-B and ADC-D form another group to oversample the output current. All ADC-A and ADC-B SOCs are triggered by the same source that is aligned with the starting point of the output voltage at t_0. SOCs from ADC-C and -D share another triggering signal at t_0' that is slightly delayed from t_0 as explained soon. Upon receiving the SOC trigger signal, SOC0 initiates the sampling and hold (S&H) process, followed by data conversion and results latching procedures. A greater numbered SOC in each module sets up its own S&H process at the end of the data conversion of the previous SOC. In this way, the assigned 14 SOCs (SOC0-SOC13) in ADC-A start their individual S&H at $t_0 - t_{13}$, accordingly and the corresponding time point of SOC0-SOC13 in ADC-C is denoted by $t_0' - t_{13}'$, thereof, the t_0' is located in the middle of t_0 and t_1, as shown in Fig. 5. By doing so, all samples from ADC-A and -C are time-evenly distributed and spliced together to represent the original signal with twice resolution for better capture of arcing-involved output voltage. The operational pattern of ADC-B and -D for output current oversampling is identical as above, and thus, is not redundantly depicted in Fig. 5. Referring to the MCU manual, the exact value of the S&H window and conversion interval for each SOC is set as 75 and 105 ns, respectively. A further shorter configuration is not recommended [26]. Consequently, it takes 180 ns in total for an ADC SOC to digitalize an analog signal upon receiving the triggering signal, followed by another 10 ns elapse before the final latch of data into the ADC result register. Therefore, in order to evenly distribute all samples from two modules, the delay between the triggering signal of ADC-A and ADC-C SOCs (or ADC-B and ADC-D) is set as 90 ns. That is to say, the time span between t_0 (t_0') and t_1 (t_1') is 180 ns, and t_0' is 90 ns lagged behind t_0, but 90 ns leads ahead t_1. The output period of the HFI at 390 kHz is around 2564 ns, thus, it allows each ADC module yield 14 samples per cycle. That is why only 14 SOCs in each module are exploited.

To control the output power, it is necessary to have both output voltage and current information, so 56 sampling data per cycle should be extracted from ADC result registers to the CPU memory before being overwritten. The bulky ADC ISR fails to accomplish such a time-tight task and, just because of this, the DMA technique is explored. It is stated in the reference manual that 1 extra system cycle is added to the beginning of each DMA burst and it takes 3 system cycles, namely, 15 ns for each DMA channel to transfer a 16-bit ADC result [26]. As a result, 215 ns is imperative to transfer all 14 sampling results yielded by a single ADC module. In total, four DMA channels are utilized and the DMA channel with a larger number will autonomically commence the data transferring task after its former completes. By setting the beginning of cycle #1 as the time origin, the exact timing arrangement of all 56 samples from 4 ADC modules (28 points for output voltage and 28 points for current sensing) along with their 4 DMA channels transferring timings are captured in Fig. 6. A signal is launched at the end of SOC12 S&H in ADC-C (or -D) module as the shared triggering source for DMA channels. Counting 1 system clock as trigger signal detection delay, the trigger signal launches the DMA-Ch1 data transferring for output voltage sensed by ADC-A at 2330 ns, followed sequentially by DMA-Ch2 for output current sensed by ADC-B at 2545 ns, DMA-Ch3 for output voltage sensed by ADC-C at 2760 ns, and DMA-Ch4 for output current sensed by ADC-D at 2975 ns. All these timing points are colored in red on the top of the time axis (t/ns) in Fig. 6 whereas the time points, implying the final latch of the ADC results, are tinted purple.

The coagulation mode features pulsating outputs and only a few output cycles are active, thereby, it is of paramount importance to extract ADC conversion data from the result register in time and save it to memory before it is overwritten by the data from the next cycle. As such, the key information contained in active cycles is preserved without losing data. As noticed in Fig. 6, the DMA-Ch1 for ADC-A data shifting is initiated at 2330 ns, and then, the transmitting process for the 14^{th} data is scheduled at 2530 ns when the conversion result of ADC-A SOC13 has already been latched into the result register. In consequence, no voltage data is missed from ADC-A. At 2545 ns, it is the time to transmit the output current data for Cycle #1 from ADC-B SOC0 to SOC13 and the data shifting execution of the 14th sampling begins at 2745 ns (as specified in gray). The new data from the ADC-B SOC0 for cycle #2 is

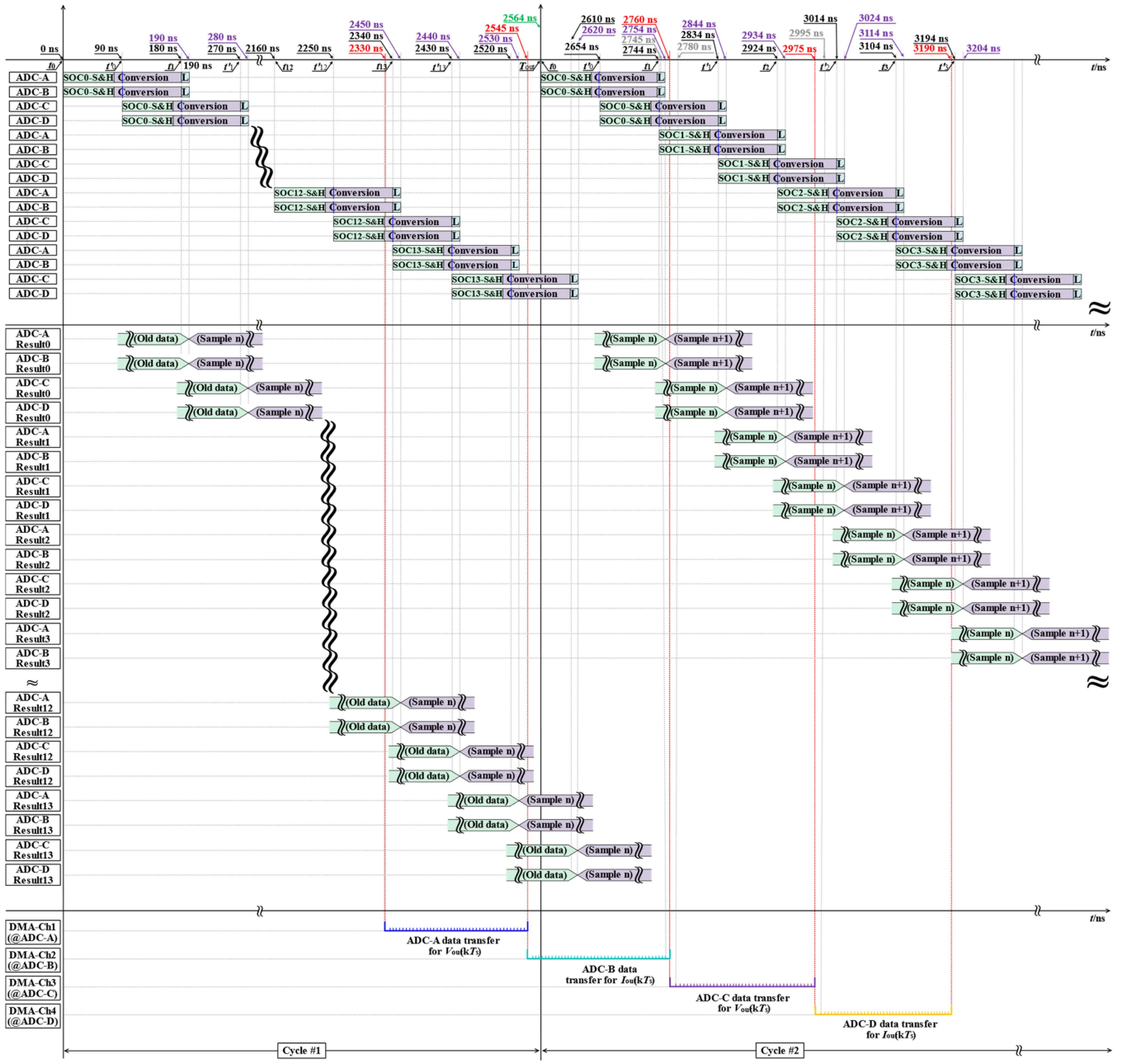

Fig. 6. ADC sampling timings and resultant data transferring using DMA. The S&Hvwindow is 75 ns while the conversion interval is 105 ns. The MCU can be configured and generates a DMA-triggering signal for data transferring at the end of "S&H" or "conversion," as pointed out by the timings in black. Additionally, it takes another 10 ns for an ADC SOC to latch the data into the result register after the conversion interval, and this is represented by a capital "L." Any reading operation before the end of data latching is returned with data from the previous cycle. The ADC SOC result is tagged by "result0-13" and the data for cycle #1 (cycle #2) is denoted as "sample n" ("sample $n+1$"). Data even earlier than cycle #1 is indicated as "old data."

not latched till 2754 ns. Consequently, data for ADC-B from Cycle #1 is completely transferred to memory by DMA-Ch2 at 2760 ns, and no data is lost. The voltage sensed by ADC-C SOC0 completes its new data latching for Cycle #2 at 2844 ns, however, the DMA-Ch3 wraps up the data shift from ADC-C SOC0 for Cycle #1 at 2780 ns. Hence, there is no data-overwriting occurred for ADC-C as well. The DMA-Ch4 for the data-transferring from ADC-D in Cycle #1 is pending till 2975 ns and all data are transferred at 3190 ns. A closer look at Fig. 6 indicates that the data point for cycle #1 from ADC-D SOC0 is not stored in the result register till 2995 ns, but the SOC result register is updated with new data for cycle #2 at 2844 ns. In this circumstance, the data for cycle #1 from the ADC-D SOC0 is overwritten. Nevertheless, it is noteworthy that the value of lost data for output current is quite small, and its impact is negligible for the following reasons. First, the output voltage, spanning across the ADC-D SOC0-S&H window, is pretty small viewing its close proximity to the zero-crossing region and such a low voltage magnitude is not able to induce air breakdown or arcing. In this case, the large impedance, originating from the air gap

between the ES tip and the target tissue, dominates and results in a small output current, thus, yielding similar SOC data value in all cycles. Second, the average output power under control is calculated over all 16 recurring cycles (448 data points in total), and then, the impact of such small-valued data is further scaled down hundreds of times, leading to trivial influence. The result register of ADC-D SOC1 is updated with data for cycle# 2 at 3024 ns, however, the DMA-Ch4 has transmitted all data for cycle #1 at 3010 ns, thus, no more data is lost. The identical data-transferring pattern continues for cycle #2, cycle #3, and so on. As discussed before, the ESG is not activated in blank periods and the outputs settle down to zero after a short transient, thus, it is not necessary to transfer all data sampled in this period to memory. In the proposed nonfixed duty cycle strategy, the number of active cycles is flexible, so the starting cycle of the blank period also varies. But, the nonfixed duty cycle is bound to be less than 31.25% (or active cycles are controlled to be less than five cycles), such that the biotissue has time to cool down, which is experimentally proved to be of the essence later. With multicycles as margins, it is determined that the data for the first half of recurring cycles (the first eight cycles) are always sent to memory whereas the data for the rest 8 blank cycles are not sent and directly treated as zero. With output sampling data stored in memory, the MCU computes the output power in blank duration and the power tracking accuracy of such a regime is experimentally checked in following sections.

III. Results With Resistive Load

A. Controllability of Duty Cycle

The proposed nonfixed duty cycle by multi-active cycles is theoretically explained in Section II-B and it is further experimentally examined here with a resistive load. The input voltage V_{in} in Fig. 2 is set as 250 V, and the resistor is directly connected to the HFI output terminals (transformer secondary side) to validate the controllability of the output duty cycle and output power tracking performance.

The controllability of the output duty cycle is showcased by well-regulated active output cycles, and three scenarios of different active cycles, i.e., one cycle, three cycles, and five cycles are exemplified and presented in Fig. 7. The output is positive if Q_1 and Q_3 in Fig. 2 are both turned ON by their gate pulses V_{gs} whereas the output is negative if Q_2 and Q_4 are ON. The HFI only outputs 1 complete cycle ($D_{\text{on}} = 6.25\%$) with a maximum output voltage of 1530 V in Fig. 7(a), and remains inactive for the rest 15 cycles. A partially zoomed figure is provided in Fig. 7(b) for better visibility. The energy stored in the HFI resonant components, such as inductors or capacitors, requires time to be dissipated, therefore, another half-cycle with sizeable output appears in all trials. However, it has no impact on output power tracking accuracy since ample sampling data for 8 cycles are transferred to MCU memory for power calculation as explained in Section II-C. In Fig. 7(c), the HFI fully outputs 3 cycles ($D_{\text{on}} = 18.75\%$) and the maximum output voltage achieves 2600 V. Similarly, Fig. 7(c) is also partially amplified as Fig. 7(d) for enhanced resolution. In Fig. 7(e) and its magnified version in Fig. 7(f), the peak voltage is further boosted to 2720

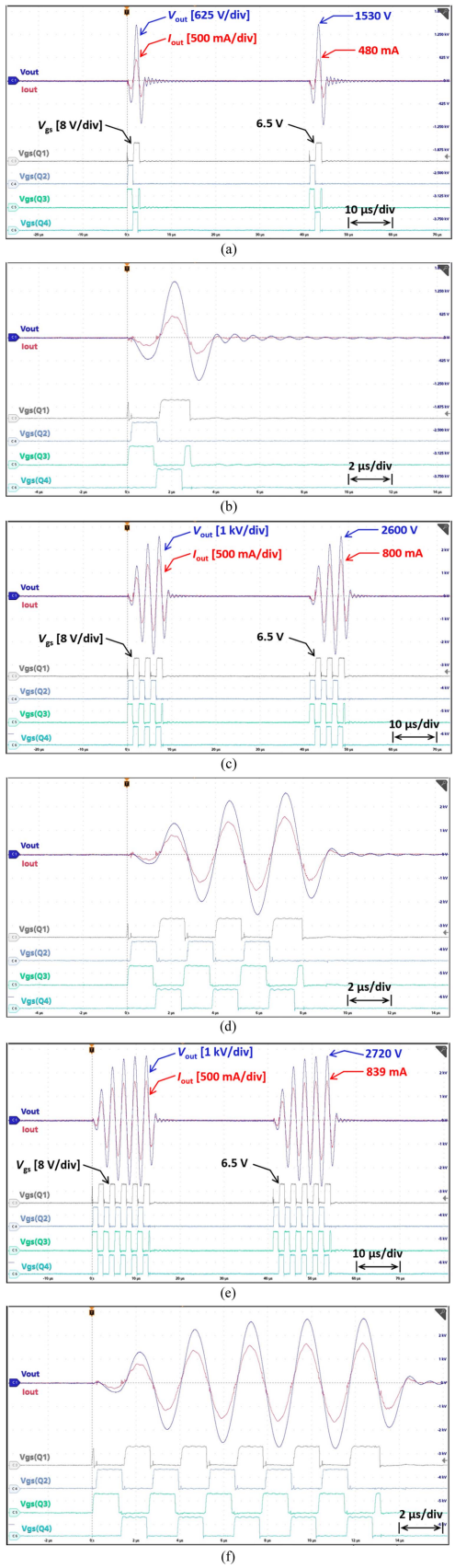

Fig. 7. Active cycle control by gate pulses V_{gs} for different duty cycles. (a) One cycle for 6.25% and partially zoomed in (b), (c) threecycles for18.75% and partially zoomed in (d), (e) five cycles for 31.25% and partially zoomed in (f).

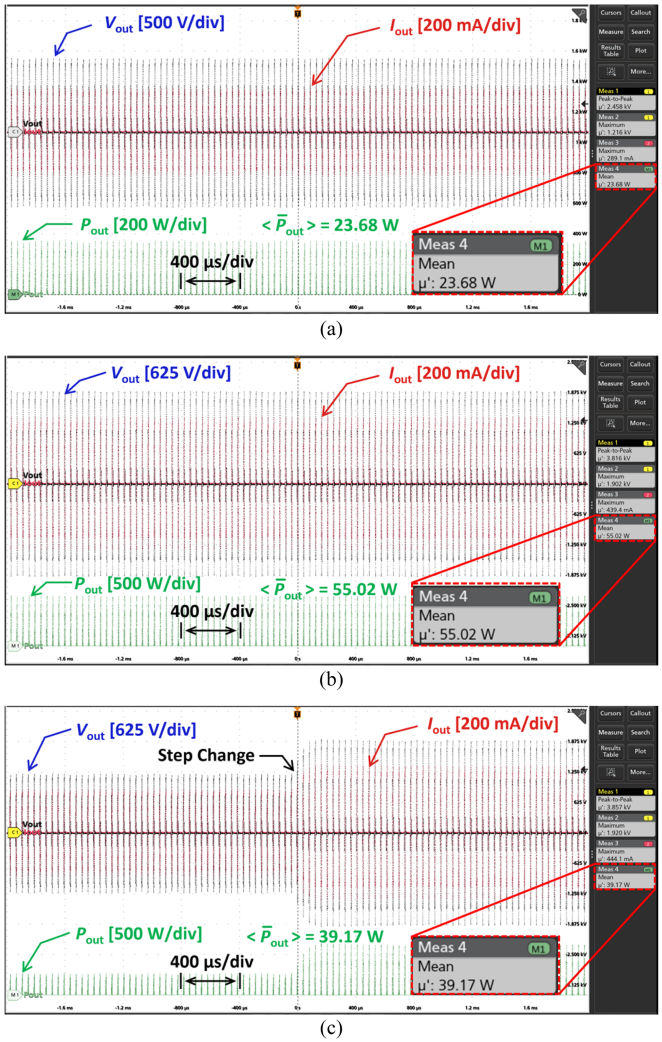

Fig. 8. Power-tracking performance of the HFI with a resistive load and 3 active output cycles. (a) 25 W. (b) 55 W. (c) Step change from 25 to 55 W.

V when the HFI delivers 5 cycles ($D_{\rm on} = 31.25\%$). As seen from Fig. 7(a)–(f), the output duty cycle is properly controlled to various discrete values, thus, the proposed nonfixed duty cycle is proved to be feasible.

B. Power Tracking Performance

The average output power over the recurring cycle is computed by utilizing the sampling data that are transferred to MCU memory by the DMA modules, as detailed in Section II-C. After that, the PI controller (see Fig. 2) is utilized to experimentally check the output power tracking performance of HFI with resistive load. The partial test results plus waveforms captured by the digital oscilloscope are provided in Fig. 8 and the overall power tracking performance is summarized in Fig. 9. For all trials reported in Fig. 8, the HFI is activated for 3 cycles ($D_{\rm on} = 18.75\%$) and the power reference is set as 25 and 55 W for Fig. 8(a) and (b), respectively. The output voltage $V_{\rm out}(t)$ is measured by Tektronix THDP0100 100 MHz differential probe and the output current $I_{\rm out}(t)$ is gauged by Tektronix TCP0030A

TABLE I
POWER CONFIGURATIONS OF DIFFERENT TESTING SCENARIOS

Active Cycles \ P_{ref}	Trials							
	#1	#2	#3	#4	#5	#6	#7	#8
One Cycle	1 W	3 W	5 W	7 W	9 W	11 W	15 W	20 W
Three Cycles	5 W	7 W	15 W	25 W	35 W	45 W	55 W	65 W
Five Cycles	15 W	25 W	35 W	55 W	75 W	95 W	115 W	130 W

120 MHz current probe. They are multiplied together by the Tektronix MSO46 oscilloscope with a 500 MHz bandwidth and 6.25 GS/s sampling speed. The resultant instantaneous power is automatically averaged over 4 milliseconds by the MSO46. The obtained average power is treated as the authentic power level delivered to the load. As seen from Fig. 8(a) and (b), with a 25 and 55 W power reference, the actual deposited output power slightly deviates and is approximately stabilized at 23.68 and 55.02 W, respectively. In Fig. 8(c), the power reference step changes from 25 to 55 W, and the HFI rapidly settles down in the new steady state in around 3∼4 recurring cycles. Therefore, it can be concluded that the HFI is able to track the power reference with small errors and prompt dynamics.

Besides the experimental tests recorded in Fig. 8, multiple tests are conducted with different amounts of active output cycles and power reference ($P_{\rm ref}$) settings, as listed and given in Table I. The HFI with one active cycle has limited capability to deposit large power to the load and is mainly designated for low power tracking to limit the output voltage stress that is documented in Section III-C. The HFI with three and five active cycles are assigned to trace medium- and high-power configurations, respectively. The power tracking performance of the tests is collectively summarized in Fig. 9. As seen from the right y-axis in Fig. 9(a)–(c), the general trend of the power tracking error in percentage falls as the $P_{\rm ref}$ for the same active cycle becomes greater. It is also noticed in Fig. 9(d) that the actual average output power $\bar{P}_{\rm out}$ tightly tracks the preset $P_{\rm ref}$ with minor errors. The maximum error is about 1.35, 1.43, and 4.92 W for one active cycle, three active cycles, and five active cycles, respectively.

To examine the power tracking performance of HFI under R–C load. A 3.2 kΩ resistor is employed to emulate actual biotissue resistance to a certain degree. The resistor is connected in parallel with a manually added 10 pF or 100 pF C0G capacitor. With the parasitic capacitance of the resistor in mind, the equivalent impedance of two R–C testing scenarios is measured by an HP-Agilent 4192A LF Impedance Analyzer which shows 3161∠-10.8° Ω and 2314∠-44.4° Ω, respectively. The power tracking performance of the R–C load is gathered in Figs. 10 and 11. It can be concluded from the data in the two figures that the overall power tracking accuracy of a fixed load with the same active cycle deteriorates as $P_{\rm ref}$ increases. Meanwhile, the tracking errors also grow when more capacitance is added to the load, as indicated by Figs. 10(d) and 11(d). Nonetheless, it is worth noting that the capacitive power angle of the R–C load herein is set way beyond the actual biotissue just to showcase the power

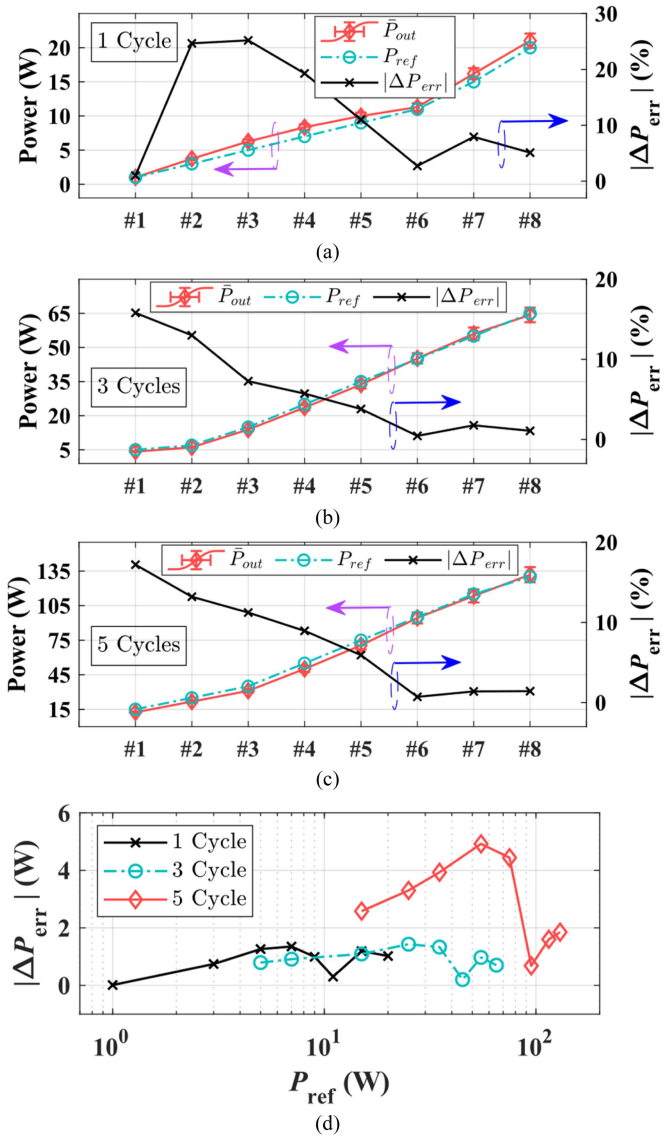

Fig. 9. Power tracking performance summation for resistive load with (a) one active cycle, (b) three active cycles, (c) five active cycles, and (d) absolute value of tracking errors.

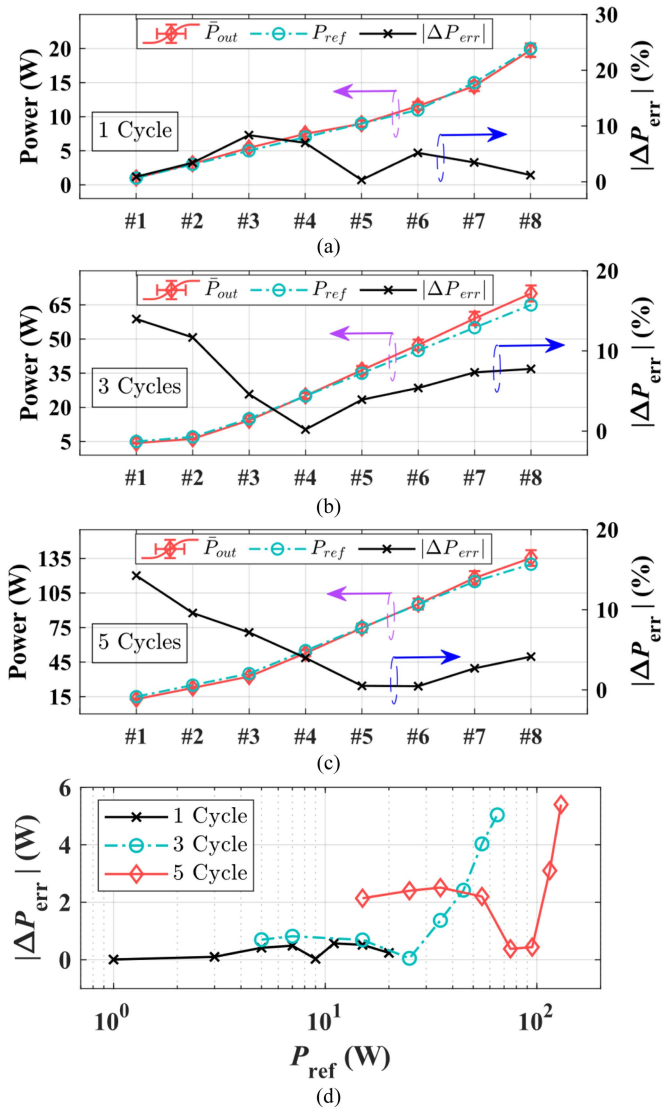

Fig. 10. Power tracking performance summation for added 10 pF in parallel with a 3.2 kΩ resistor. (a) One active cycle, (b) three active cycles, (c) five active cycles, and (d) absolute value of tracking errors.

tracking performance. The power tracking accuracy with fresh muscle tissue as the load is presented in Section IV-A.

C. Efficacy of the Nonfixed Duty Cycle

The maximum output voltage magnitude ($V_{\text{mag-max}}$) for trials in Table I with a resistive load is measured across the transformer's secondary side and recorded. The secured data are semilogarithmically plotted versus the actual output power in Fig. 12(a). It is observed that, to deliver the same amount of power, the $V_{\text{mag-max}}$ is significantly reduced by more active cycles. Hence, it lowers the chance of accident air breakdown and thus, reduces the potential of alternative thermal injury sites for safety improvement. In other words, the HFI with fewer active cycles features a higher $V_{\text{mag-max}}$ that elicits a larger terminal leakage as delineated in Fig. 12(b). Fig. 12(c) reveals that, compared to trials with fewer active cycles, the terminal leakage current measured from the transformer secondary side of the HFI is smaller for those with more activated cycles when the output power levels are identically set. This observation motivates and leads authors to the proposal of the nonfixed duty cycle (or multiple active cycles) for coagulation mode with reduced terminal leakage current and enhanced safety.

IV. Results With Biotissue Load

A. Power Tracking Performance

Experiments with the same settings listed in Table I are repeated with fresh pork as biotissue load for the same HFI setup used for resistive load. In those duplicated tests, the pork is placed on the return pad, however, the pork surface does not directly contact the ES, which means there is always an air gap

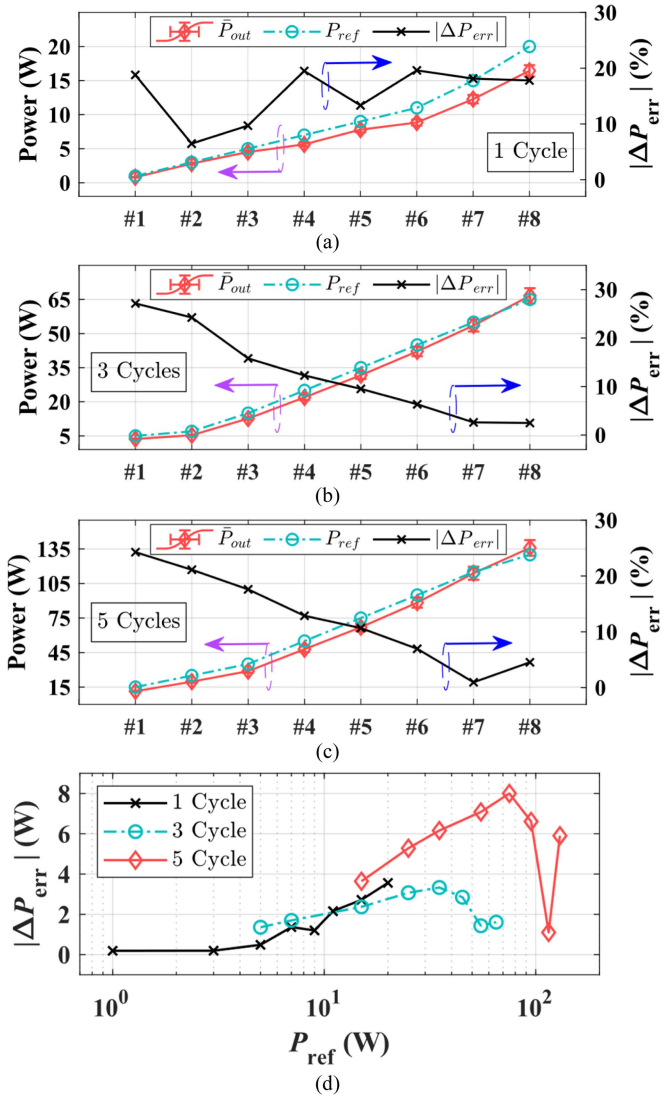

Fig. 11. Power tracking performance summation for added 100 pF in parallel with a 3.2 kΩ resistor. (a) One active cycle, (b) three active cycles, (c) five active cycles, and (d) absolute value of tracking errors.

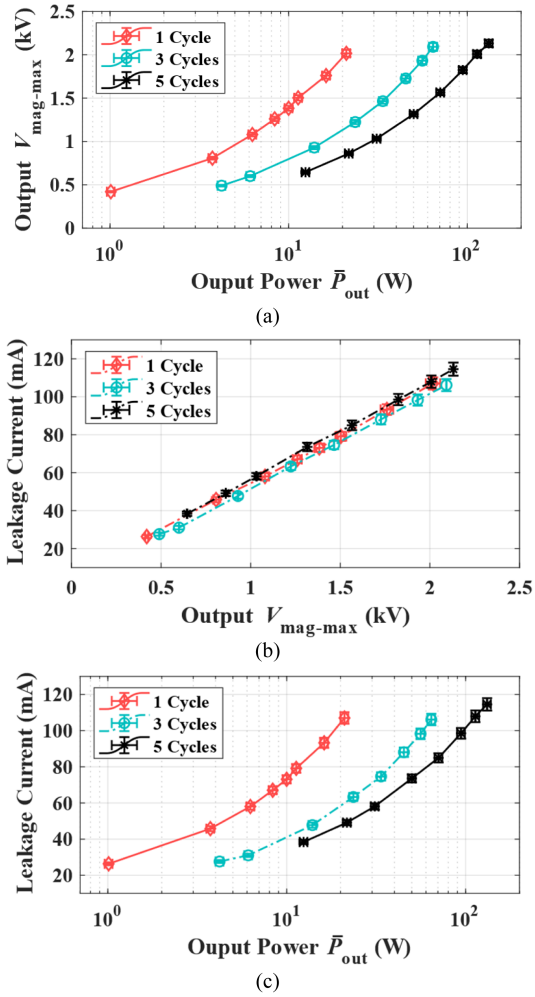

Fig. 12. Relationship among average output power, maximum output voltage magnitude, and terminal leakage current. (a) $V_{\text{mag-max}}$ versus $\bar{P}_{\text{out}}$. (b) The terminal leakage current versus $V_{\text{mag-max}}$. (c) Leakage current versus $\bar{P}_{\text{out}}$.

lying between the pork surface and the tip of the ES. The energy from the HFI is not delivered to the pork unless the arcing (or plasma channel) is formed by ionized air. Viewing that, a damping resistor in parallel with output is usually needed to consume the stored resonant energy when HFI is connected to biotissue load. The appearance of arcing introduces significant nonlinearity to the circuitry and thus, both the output voltage and current are heavily distorted as manifested in Fig. 13. The HFI with one active cycle is set to track a power reference of 15 W in Fig. 13(a), and the output voltage (blue trace) and current (red trace) waveforms are partially provided. The output waveforms for 3 active cycles with P_{ref} as 35 W, and five active cycles with P_{ref} as 55 W P_{ref} are fragmentarily offered in Fig. 13(b) and (c), respectively. It is clear from the annotations that the summit of output voltage for each case in Fig. 13 is of a close magnitude.

Hence, the terminal leakage current will be of a similar level as indicated by Fig. 12(b). However, the output power delivered to the biotissue load differs a lot. Therefore, it can be concluded that, contrasted to the case with fewer active cycles, the HFI with more active cycles lifts the achievable power level when the output voltage stress or terminal leakage current is at a comparable level. On the opposite side, if the delivered power is maintained the same, then the maximum output voltage amplitude and the terminal leakage will be less for the case with more cycles, which contributes to a safer coagulation mode.

As noticed from Fig. 13, the output voltage is highly distorted, and it is not sinusoid with low THD anymore. So, compared to the attained accuracy for resistive load, the attainable power accuracy is expected to be lower for the pork load by reason of the involvement of electrical arcing. The power tracking performance of duplicated testing for the pork is gathered and graphed in Fig. 14. The power tracking errors are relatively small when the HFI only outputs 1 active cycle and the maximum errors are 1.03 W in Fig. 14(a). The maximum tracking error for three active cycles is 4.87 W in Fig. 14(b) and it occurs in scenario #8 with P_{ref} as 65 W. The averaged output power of only one active cycle can hardly go high, because of that, its

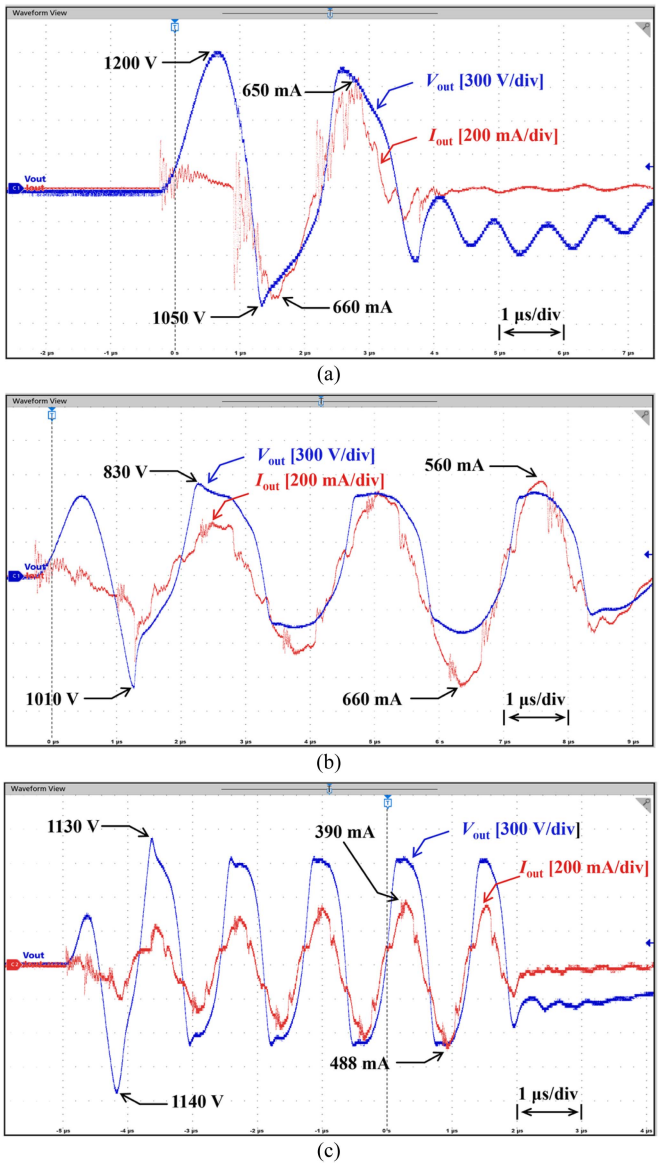

Fig. 13. Output waveforms for fresh pork load with a power reference of (a) 15 W by one active cycle, (b) 35 W by three active cycles, and (c) 55 W by five active cycles.

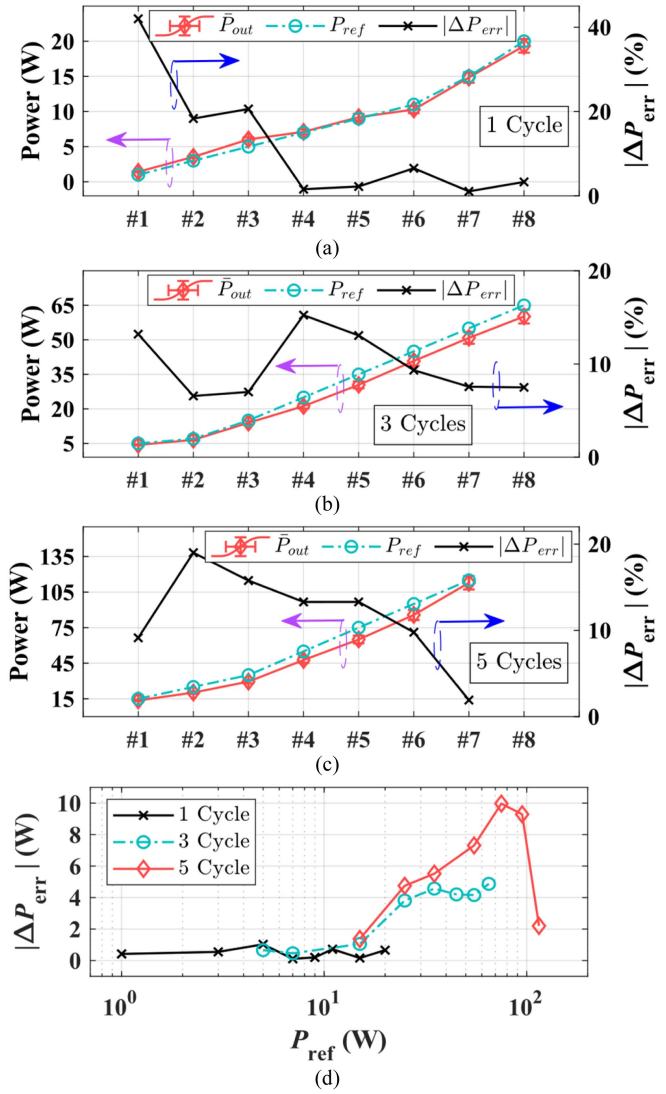

Fig. 14. Power tracking performance for biotissue load with (a) one active cycle, (b) three active cycles, (c) five active cycles, and (d) absolute value of tracking errors.

maximum setting is clamped at 20 W. Meantime, as the P_{ref} exceeds 115 W in trial #7, the stainless-steel ES begins to melt, secondary to the lack of sufficient blank periods for cooling, so trial #8 set at 130 W is skipped to avoid damaging the ES. The peak tracking errors for all tested cases of five active cycles rise to 9.97 W in Fig. 14(c) and it happens in scenario #5 with a 75 W as the tracking reference. When compared to Fig. 9(d), it is found that the overall tracking errors slightly increase in Fig. 14(d) but are still at a preferred level against the accuracy reported in existing commercial ESGs [8]. Viewing distortions appearing in the output, the increased tracking errors seen in Fig. 14 are predictable since only 28 ADC sampling points are available for output voltage or current. If tracking errors are supposed to be further reduced in the target applications, then, extra fast ADCs with a sampling speed of tens of MHz or so, together with faster digital processors, e.g., FPGA, with a system clock of sub-GHz or GHz is required. But the overall cost, system complexity, and coding challenges typically become higher. Furthermore, when designing such a high-speed system, special attention is needed for printed circuit board layout, electro-radiation shielding, communication interface design, electromagnetic interference prevention, etc.

With the acquired power tracking performance, nine trials with different active cycles and power reference settings, as given in Table II, are conducted on fresh pork by the authors. Among all traces, trace #1∼#3, trace #4∼#6, and trace #7∼#9 are induced by different powers with one, three, or five active cycles, respectively. Trace #2 and #4; trace #3, #5, and #7; and trace #6 and #8, are intentionally configured with the same power references but different active pulses. With such an arrangement, it is convenient to compare coagulation effects either by different

TABLE II
TRIAL SETTINGS FOR 9 COAGULATION TRACES

Trials / Power Setting	Test Scenarios								
	1 Active Cycle			3 Active Cycles			5 Active Cycles		
	Trace #1	Trace #2	Trace #3	Trace #4	Trace #5	Trace #6	Trace #7	Trace #8	Trace #9
P_{ref}	1 W	7 W	15 W	7 W	15 W	35 W	15 W	35 W	55 W

power settings but the same active pulses, or by the same power setting but different active pulses.

The obtained coagulation effect in each trial is photographed and presented in Fig. 15(a). Inspecting all traces, it is not hard to find that the width of coagulation traces tends to be wider with a darker hue as the applied power rises. For instance, the coagulated width of trace #1 is less than that of trace #2. Trace #3 has the largest trace width among trace #1∼#3. A similar truth is held for trace #4∼#5 and trace #7∼#9 as well. In general, the color of traces tends to be darker as power levels increase. In addition, in contrast to a wide superficially coagulated spread region shown later in Fig. 16(d), the spread area here is limited to a narrow width. The traces yielded by the same power setting but different active cycle quantities, appear to be similar in terms of trace width and hue, which justifies the proposal of the nonfixed duty cycle again for its similar coagulative effect but lower leakage current and output voltage stress. Trace #1 in Fig. 15 has the lowest power setting among all traces and such power barely coagulates the pork while the output power is oversized for trace #9. Therefore, substantial tissue carbonization occurs with the presence of black scars. From Fig. 15(a), it can be stated that the proper power selection for a certain biotissue during clinical surgery is of paramount importance. The power in actual electrosurgery is usually selected by professional surgeons with extensive experience gained from training or clinical practice. None of the authors is a surgeon and the power settings given in Tables I or II are chosen without any clinical consideration. Besides that, the operation skill of operators is another factor posing a crucial impact on the final coagulation effects, and the authors do not receive any professional electrosurgical operation training, which may compromise the final achieved coagulation quality.

As mentioned earlier, electrical arcing routinely appears in coagulation mode due to air breakdown by the high electrical field intensity. A momentary snapshot of arcing taken from trial #6 is displayed in Fig. 15(b) and (c) for the top and left-side views, respectively. For the purpose of bettering the visuality, the orientation of the pork is marked in Fig. 15 as well.

B. Importance of Blank Periods

It is said in Fig. 1 that the arcing-involved coagulation mode requires pulsating output, and the blank period is critical to sufficiently cool down the temperature of the biotissue near the coagulating site. In order to justify this statement, a continuous output voltage with no blank period is applied to the pork with a peak-to-peak amplitude of 4.5 kV. The applied high voltage

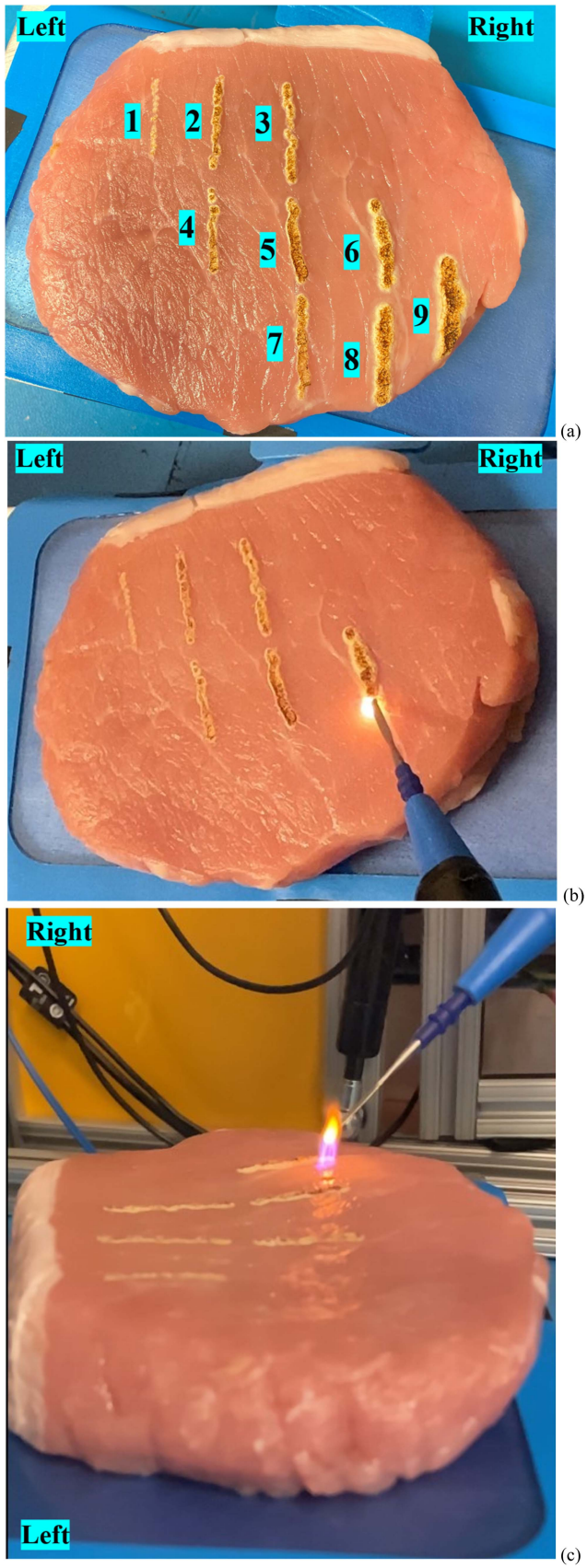

Fig. 15. Capture of coagulation traces and electrical arcing. (a) Top view of all traces, (b) top- and (c) left-side view of electrical arcing from trial #6.

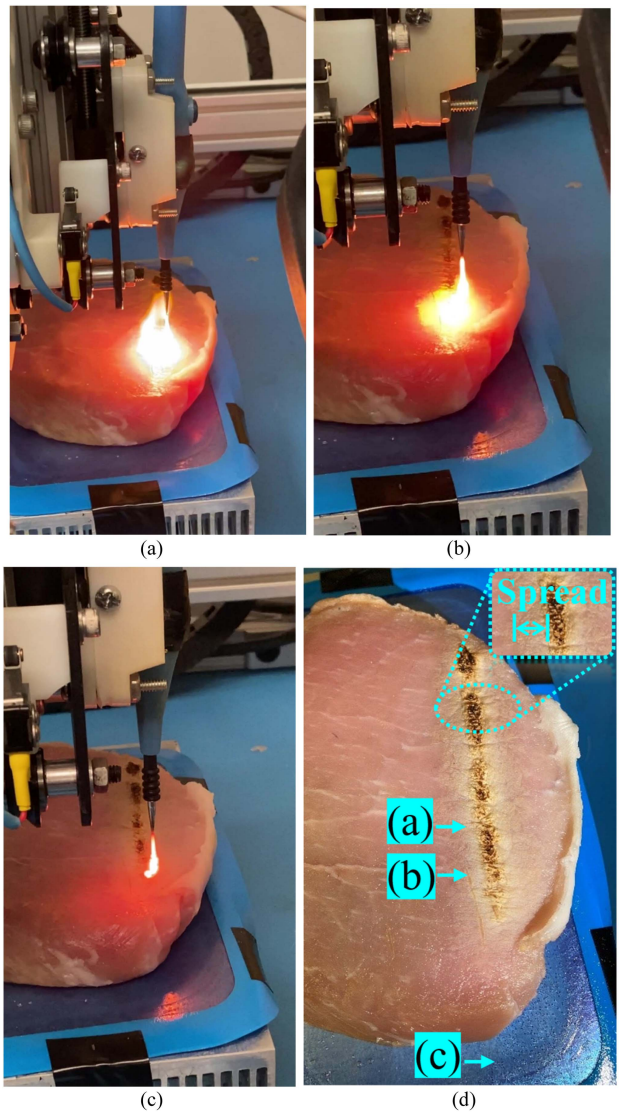

Fig. 16. Electrical arcing around the ES at (a) location #1, (b) location #2. (c) Melted stainless-steel electro scalpel attributed to a high temperature that exceeds its melting point at around 1400 °C. (d) Carbonization and denaturation of tissue that is induced by the continuous output without blank periods. The location of ES in early subfigures (a)–(c) Labeled with a matching lowercase letter and the moving direction of the ES in this trial is pointing from (a) to (c).

continuously creates a mass of randomly flickering arcing with considerable volume in all directions. This arcing or ionized air forms a high-temperature plasma cloud that is sprayed on a large surface area of the pork, like a falling-down waterfall, as caught by Fig. 16(a) and (b). The temperature of the arching is so high that the tip of the stainless-steel ES is overheated and sparkles reddish and white light. Eventually, the tip melts in Fig. 16(c) as a result of the lack of blank periods for cooling.

Such a high-temperature sprayed plasma cloud not only carbonizes the pork a lot and leaves a black hue along the planned coagulation trace, but also invokes a superficial denaturation layer over an extensively spread and uncontrolled area, as shown in Fig. 16(d).

The size of the electrical arcing in Fig. 15, induced by the output voltage with the presence of blank periods, shrinks a lot when in comparison with arcing here in Fig. 16. In such a manner, it can be said that the blank periods help suppress the spread of superficially coagulated regions. For that reason, in order to achieve a more controllable coagulated zone with the shrunk thermal spread area, the biotissue temperature should be confined by pulsating the output wherein the continuous high voltage is interrupted and interweaved by a blank period. By doing so, the air breakdown only happens when high voltage is present. The resulting current in active cycles rapidly heats and desiccates the local biotissue, causing a prompt rise in both regional thermal resistance and the total circuit impedance. The increased tissue impedance reduces the circuit current and prevents further excessive heat generation while the augmented thermal resistance attenuates the propagation of the thermal effect to the deeper layer of biotissue. During blank periods, the air retains its isolation intensity, and no energy is transmitted to the biotissue. It not only allows the tissue temperature to cool down but also helps with reducing the arcing volume as well as random arcing flickers, which narrows the thermal spread width and assists a more consistent denatured region. Therefore, it is essential to have blank periods together with active periods for a desired coagulation mode.

V. Conclusion

This article comprehensively introduces the arcing-involved pulsating coagulation mode for electrosurgery and originally investigates an industrial-scale low-speed MCU-based solution to tackle the challenges of implementing such a mode. In the proposed GaN-based prototype, a 200 MHz low-speed MCU is employed to exemplify the output sampling and data-transferring strategy. The output sampling and resultant data transferring are finished without intervention from the CPU, such that a low-speed MCU is qualified to compute average output power during blank periods and realize ultrafast real-time power control. The power tracking performance is experimentally scrutinized and summarized for resistive load, *R*–*C* load, and biotissue load. The power tracking errors for the biotissue load are slightly higher than that of the resistive load. Among all trials, maximum power tracking errors are 4.92 and 9.97 W for resistive and biotissue load, respectively. The safety concerns of using pulsating coagulation mode concerning alternative thermally injured sites or terminal leakage current caused by high output voltage, are addressed by the novel nonfixed duty cycle control scheme. The controllability of the nonfixed duty cycle is validated by the developed hardware prototype, and it is proved that the duty cycle can be accurately controlled to a discrete value by varying the number of active cycles. Under constraints of terminal leakage current, the active cycle of a small quantity is more suitable for cases requiring low power while a large number of active cycles are preferred for cases needing large power settings. At the end of the article, the existence of blank periods in terms of narrowing thermal spread and reducing tissue carbonization is proved to be crucial. It is found that, without blank periods, wide thermal spreads are observed together with significant carbonization.

This article is the first that articulates detailed circuitry implementation of electrosurgical pulsating coagulation mode. It features small power-tracking errors, and achieves enhanced safety through a nonfixed duty cycle strategy with reduced output voltage amplitude and shrunk terminal leakage current. Therefore, this article may promote further electrosurgical research toward a safer coagulation mode with higher simplicity but lower cost.

ACKNOWLEDGMENT

The content is solely the responsibility of the authors and does not necessarily represent the official views of the National Institutes of Health.

REFERENCES

[1] D. Wang et al., "Soft coagulation monopolar suction for rapid resection of supratentorial brain tumors: Feasibility of a new technique and outcomes," *World Neurosur.*, vol. 163, pp. e137–e145, Jul. 2022.
[2] A. Uchiyama, K. Miyoshi, and K. Nakamura, "VIO soft-coagulation system for major pulmonary resections: Results in 68 patients with primary lung cancer," *Gen. Thoracic Cardiovasc. Surg.*, vol. 59, no. 3, pp. 175–178, Mar. 2011.
[3] M. Miyazawa et al., "Laparoscopic liver resection using a monopolar soft-coagulation device to provide maximum intraoperative bleeding control for the treatment of hepatocellular carcinoma," *Surg. Endoscopy*, vol. 32, no. 4, pp. 2157–2158, Apr. 2018.
[4] M. L. Morris and J. H. Hwang, "Electrosurgery in therapeutic endoscopy," in *Clinical Gastrointestinal Endoscopy*, 3rd. Ed., Elsevier, 2019, pp. 69–80.e2.
[5] L. Feldman, P. Fuchshuber, and D. B. Jones, *The SAGES Manual on the Fundamental Use of Surgical Energy (FUSE)*. Berlin, Germany: Springer, 2012.
[6] International Electrotechnical Commission(IEC.), "Medical electrical equipment - Part 2-2: Particular requirements for the basic safety and essential performance of high frequency surgical equipment and high frequency surgical accessories," 2017. [Online]. Available: https://webstore.iec.ch/publication/28118/
[7] N. N. Massarweh, N. Cosgriff, and D. P. Slakey, "Electrosurgery: History, principles, and current and future uses," *J. Amer. College Surgeons*, vol. 202, no. 3, pp. 520–530, Mar. 2006.
[8] "User's guide Valleylab FT10 FT series energy platform," 2015. [Online]. Available: https://www.manualslib.com/manual/1663078/Covidien-Valleylab-Ft-Series.html
[9] "HF generator ESG-400 - Olympus medical systems," 2020. [Online]. Available: https://www.olympus-europa.com/medical/en/Products-and-Solutions/Products/Product/ESG-400.html/
[10] P. Mock, "VIO 300 D user manual," 2004. [Online]. Available: https://www.manualslib.com/manual/1335514/Erbe-Vio-300-D.html/
[11] "VIO 3 Precise, reliable, reproducible," Jul. 2020. [Online]. Available: https://us.erbe-med.com/fileadmin/user_upload/MKT5072_VIO-3_2020-07_low-res.pdf/
[12] L. Liu, Y. Li, and L. Gu, "Multiphase interleaved reconfigurable high-frequency-voltage inverter for electrosurgical generator," in *Proc. IEEE Energy Convers. Congr. Expo.*, 2022, pp. 1–5.
[13] Z. Jin and L. Gu, "Combined feedforward duty cycle predictive and feedback power control for electrosurgical generator," in *Proc. IEEE Energy Convers. Congr. Expo.*, 2023, pp. 5151–5155.
[14] S. Jensen and D. Maksimovic, "Fast tracking electrosurgical generator using two-rail multiphase buck converter with GaN switches," *IEEE Trans. Power Electron.*, vol. 32, no. 1, pp. 634–641, Jan. 2017.
[15] B. Yoon et al., "4 MHz electrosurgical generator system for wide load impedance range with SiC-based full-bridge inverter," *IEEE Trans. Ind. Electron.*, vol. 71, no. 1, pp. 338–347, Jan. 2024.
[16] S. Jensen, L. Corradini, M. Rodriguez, and D. Maksimovic, "Modeling and digital control of LCLC resonant inverter with varying load," in *Proc. IEEE Energy Convers. Congr. Expo.*, 2011, pp. 3823–3829.
[17] C. Bao and S. K. Mazumder, "Multiresonant-frequency filter for an electrosurgery inverter," *IEEE Trans. Power Electron.*, vol. 37, no. 6, pp. 6242–6246, Jun. 2022.
[18] C. Bao and S. K. Mazumder, "Reduced collateral tissue damage using thermal-feedback-based power adaptation of an electrosurgery inverter," *IEEE Trans. Power Electron.*, vol. 37, no. 10, pp. 11540–11545, Oct. 2022.
[19] C. Bao and S. K. Mazumder, "Output power computation and adaptation strategy of an electrosurgery inverter for reduced collateral tissue damage," *IEEE Trans. Biomed. Eng.*, vol. 70, no. 6, pp. 1729–1740, Jun. 2023.
[20] S. K. Mazumder, C. Bao, H. El-Kebir, Y. Lee, J. Bentsman, and R. Berlin, "Electrosurgery power electronics: A revolution in the making," in *Proc. IEEE Appl. Power Electron. Conf. Expo.*, 2023, pp. 692–698.
[21] D. A. Friedrichs, R. W. Erickson, and J. Gilbert, "A new dual current-mode controller improves power regulation in electrosurgical generators," *IEEE Trans. Biomed. Circuits Syst.*, vol. 6, no. 1, pp. 39–44, Feb. 2012.
[22] C. Bao and S. K. Mazumder, "GaN-HEMT based very-high-frequency ac power supply for electrosurgery," in *Proc. IEEE Appl. Power Electron. Conf. Expo.*, 2021, pp. 220–225.
[23] A. I. Brill, "Energy-based techniques to ensure hemostasis and limit damage during laparoscopy," May 2003. [Online]. Available: https://www.mdedge.com/obgyn/article/61365/energy-based-techniques-ensure-hemostasis-and-limit-damage-during-laparoscopy/
[24] S. K. Mazumder, C. Bao, and A. I. Mehta, "Power-electronics enabled precision-power electrosurgery," *IEEE Power Electron. Mag.*, vol. 10, no. 4, pp. 20–25, Dec. 2023.
[25] B. Schneider and P. J. Abatti, "Electrical characteristics of the sparks produced by electrosurgical devices," *IEEE Trans. Biomed. Eng.*, vol. 55, no. 2, pp. 589–593, Feb. 2008.
[26] "TMS320F2837xD dual-core microcontrollers technical reference manual," 2013. [Online]. Available: www.ti.com/

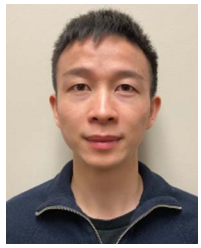

Congbo Bao (Graduate Student Member, IEEE) received the B.S. degree in electrical engineering from Huaiyin Normal University, Huai'an, China, in 2016, and the M.S. degree in electrical engineering from China University of Mining and Technology, Xuzhou, China, in 2019, and the Ph.D. degree in electrical and computer engineering from the University of Illinois Chicago, Chicago, IL, USA, in 2024.

He has more than five years of hands-on experience in designing, testing, and debugging wide bandgap-based high-frequency inverters/converters, and he has been with Hitachi Energy, Tarrs, PA, USA, since March 2024. His research focuses on developing novel power electronics circuitry and control for safer electrosurgery with enhanced clinical quality.

Sudip K. Mazumder (Fellow, IEEE) received the Ph.D. degree in electrical and computer engineering from Virginia Tech, Blacksburg, VA, USA, in 2001.

He is currently a UIC Distinguished Professor and is the Director of Laboratory for Energy and Switching-Electronic Systems, Department of Electrical and Computer Engineering at the University of Illinois Chicago, Chicago, IL, USA. He has more than 30 years of professional experience and has held R&D and design positions in leading industrial organizations and has served as technical consultant for several industries. He is currently with the President of NextWatt LLC, Hoffman Estates, IL, USA.

Dr. Mazumder was a Fellow of the American Association for the Advancement of Science, in 2020, and a Fellow of the Asia-Pacific Artificial Intelligence Association in 2022. He has been the Editor in large for the IEEE Transactions on Power Electronics since 2019 and was an IEEE Distinguished Lecturer from 2016 to2019. He has been an Administrative Committee Member for IEEE PELS, since 2015. He has also been a Member-at-Large for IEEE PELS, since 2020. He was the Chair for the IEEE PELS Technical Committee on Sustainable Energy Systems, from 2015 to 2020. He was the General Chair for IEEE PEDG Conference in 2023 and is currently the General Co-Chair for IEEE Energy Conversion Congress & Exposition in 2024. He is the recipient of the 2023 IEEE Power & Energy Society's Ramakumar Family Renewable Energy Excellence Award. He was also the recipient of several IEEE awards/honors, including IEEE Transactions on Power Electronics Prize Paper Awards (2022, 2002) and Highlighted Papers (2023, 2022, and 2018), Featured Article for IEEE TRANSACTIONS ON BIOMEDICAL ENGINEERING (2023), IEEE Conference Best Paper Award (2013), and IEEE International Future Energy Challenge Award (2005).